

The effect of composition on microstructure and properties for additively manufactured superalloy 718

Timothy M. Smith^{1*}, Timothy P. Gabb¹, Christopher A. Kantzos¹, Aaron C. Thompson², Chantal K. Sudbrack³, Brian West⁴, David L. Ellis¹, Cheryl L. Bowman¹

¹NASA Glenn Research Center, Cleveland OH 44135 USA

²Vantage Partners; 3000 Aerospace Pkwy, Brook Park OH 44142, USA

³National Energy Technology Laboratory, Albany OR 97321, USA

⁴NASA Marshall Space Flight Center, Huntsville AL 35808 USA

*email: timothy.m.smith@nasa.gov

ABSTRACT

Additive manufacturing (AM) represents an exciting new approach towards producing metallic aerospace components. The ability to make complex geometries that were impossible to create using conventional manufacturing methods has sparked interest from the aerospace community, including NASA. The use of AM components for crucial and human rated space missions necessitates a full characterization of the differences between AM and more conventional wrought and cast processes. For this study, sixteen different commercially available superalloy 718 powder feedstocks were obtained, built using laser powder bed fusion (L-PBF), and microstructurally and mechanically analyzed. These measurements revealed a wide range of build qualities and microstructures despite all powder lots falling within the 718 chemical specification and being processed using the same prescribed build and heat treatment parameters. Statistical analysis found a strong correlation of the amount of carbon in the powder with the final grain size and strength of the heat-treated 718 part. Ultimately, this study highlights the need of a refined superalloy 718 chemical specification for powder lots to be used in AM.

Keywords: Superalloy 718, Additive Manufacturing, Properties, Microstructure, Composition

1. Introduction

The National aeronautics and space administration (NASA) is currently establishing standards and procedures for the use of additively manufactured (AM) components for space flight missions. However, the acceptance of AM processed parts is predicated on the knowledge that AM processing does not produce material equivalent to wrought or cast processing and therefore a higher degree of fabrication and component screening is required. One alloy that has been established as a promising candidate for laser powder bed fusion (L-PBF) is superalloy 718 (“718”) [1–5]. This workhorse, medium temperature alloy has been widely used for decades in many energy and aerospace applications due to its balance of stable mechanical properties for a wide range of temperatures, modest cost, and amenability to fabrication processes such as welding [6–8]. It’s weldability may also explain its success in AM processes such as L-PBF [9–11]. L-PBF fabrication optimized for 718 can generally keep part porosity below 0.5% [1,3,12–17]. Still, AM parts destined for critical applications may undergo a hot isostatic pressurization (HIP) heat treatment step to remove the remaining porosity and inherent grain structure anisotropy [18,19]. This HIP step improves the predictability of final parts performance by homogenizing and recrystallizing the grain structure and by minimizing porosity [20–22]. Currently, it is not clear whether the chemical and heat treatment standards used for conventional wrought 718 are optimum, especially when a HIP processing step is included [23]. In fact, recent studies have found that the specified heat treatment of wrought 718 may not be optimal for parts produced using AM [24–26]. A recent study by Hovig et al. [27] and Wang et al. [4] denoted that the ductility of AM 718 could be drastically different

depending on the heat treatment parameters used and precipitation formation observed. Both studies found this change in ductility to be attributed to the amount of δ phase present. In fact, numerous studies have been conducted on AM 718 to better understand and optimize its mechanical and microstructural properties after different heat treatments [8,14,15,22,25,28–33]. However, these studies almost always investigated one 718 composition, master heat, and/or powder lot at a time. As a consequence, the effect subtle differences in powder chemistry might have on the AM process and build quality is not clear [28,34–36]. Moreover, many of these studies did not measure how different heat treatments effected important minor phases, such as carbides [25].

Therefore, the objective of this study was to investigate 16 different commercially available 718 powder lots that were processed using the same AM build and post processing steps to explore if subtle powder characteristic or compositional differences could affect the final mechanical properties of the AM component. For this study, microstructural and mechanical properties were quantified for each build, including average porosity (as-built and post thermal processing), average grain diameters, and room temperature tensile results. These measurements found a wide range of build qualities and microstructures despite all powder lots falling within the 718 chemical specification [23] and being processed using the same prescribed build and heat treatment parameters. Statistical analysis found a strong correlation between the amount of carbon in the powder and the final grain size and tensile strength of the heat-treated 718 part. Through extensive microstructural characterization and thermodynamic modeling, it is believed that elevated amounts of carbon combined with additional post-processing steps required for AM 718, promotes the formation of MC carbides over more

crucial intermetallic phases such as δ , γ' , and γ'' . Therefore, this study reveals the need for a refined chemical specification for Inconel 718 which targets metal AM fabrication.

2. Experimental section

2.1 Superalloy 718 powder feedstock (chemistry)

For this study, sixteen different 718 powder lots were purchased from five different vendors (denoted by numbers). Variations between vendor lot may consist of slightly different powder cut sizes or time of purchase and are denoted by different letters. Powder lot size and circularity was quantified using a Malvern Morphologi G3SE system to image a minimum 20,000 individual powder particles per scan with transmitted illumination, automated optical image collection, scan area with 25 mm diameter, and a minimum particle diameter of 7 μ m. Presented D_{10} , D_{50} , D_{90} measured powder size values refer to the particle diameters corresponding to the 10%, 50%, 90% cumulative powder size distribution values. Circularity of the powder was calculated using the below equation where a perfectly circular particle would equal 1.

$$Circularity = \frac{4 \times \pi \times area}{Perimeter^2} \quad (1)$$

All vendor size ranges fell within the 10 μ m - 45 μ m diameter range, which is the size distribution recommended for L-PBF and were all atomized in argon. The chemical composition for all 16 feedstocks, shown in Table 1, were measured using an average of two analyses by a LECO CS-444-LS carbon/sulfur determinator, a LECO TC-436 N/O determinator, and a Varian Vista Pro Inductively Coupled Plasma (ICP) Emission Spectrometer for boron and the metallic

elements. The expected error of the chemical measurements is around $\pm 2\%$. To ensure accuracy, all elements were measured including Ni and Fe.

Table 1: Superalloy 718 chemistries in weight percent

ID	Al	Cr	Fe	Mo	Nb	Ni	Ti	C	N (ppm)	O (ppm)
Specs	0.2-0.8	17-21	Bal.	2.8-3.3	4.8-5.5	50-55	0.7-1.2	.08 max	-----	-----
1a	0.4	18.82	18.25	2.96	5.16	53.1	0.88	0.035	325	181
1b	0.51	18.94	19.06	3.03	4.8	52.7	0.81	0.024	87	240
1c	0.38	18.17	18.19	2.94	5.2	53.6	0.98	0.028	331	182
2a	0.47	19	19.03	3.04	5.17	52.4	0.86	0.005	25	158
2b	0.41	18.85	18.84	2.98	5.06	52.8	0.89	0.006	46	162
3a	0.48	19.02	18.97	3.04	4.91	52.4	0.92	0.033	122	165
3b	0.5	19.11	18.54	2.96	4.93	52.9	0.82	0.028	331	182
3c	0.69	18.38	19.12	2.98	4.98	52.25	0.88	0.036	176	210
4a	0.35	18.25	18.19	2.97	5.11	53.7	0.94	0.029	472	176
4b	0.39	18.37	18.46	2.97	4.97	53.6	0.92	0.039	370	109
4c	0.39	18.22	18.24	2.94	4.96	53.95	0.92	0.033	607	166
4d	0.31	19.5	17.0	3.06	5.37	53.71	1.0	0.06	100	100
5a	0.46	18.78	18.11	2.99	5	53.6	0.94	0.036	207	210
5b	0.49	18.77	18.15	3.02	5.08	53.4	0.92	0.039	176	171
5c	0.45	19.09	18.02	3.01	5.04	53.3	0.93	0.024	267	215
5d	0.47	19.02	17.98	2.98	5.02	53.4	0.91	0.021	234	202

The powder lots from table 1 all fall within the AMS 5664F compositional specifications for 718 [23] but represent significant variations within this range. Each powder lot was then used to produce bars and characterization pieces via L-PBF.

2.2 AM build and post-processing

Build sets from each powder lot were produced on a Concept Laser M1 L-PBF machine at NASA Marshall Space Flight Center (MSFC) equipped with a custom-built small-volume build box (100 mm x 100 mm x 80 mm) using a 30 μm build-layer thickness and customized parameters that are optimized from Concept Laser's recommended parameters for 718. The

builds used a cross-hatching scan strategy with the scanning direction altered by 90° between consecutive layers. Each build also employed a contour scan on the perimeter to heal porosity associated with turning points. Each build set included at least nine net-shape or near-net shaped mechanical test bars (7 fatigue and 2 tensile), nominally 80 mm x 15 mm, and two full-height microstructure-characterization bars, nominally 80 mm x 25 mm x 6.4 mm. Each sample type was produced at the exact same area in the build plate for each powder lot. The bars were built with a taper and were removed from the build plate without stress relief. One microstructure-characterization piece was used to analyze the as-built microstructure while another went through the complete thermal post-processing procedure. Thermal post-processing consisted of hot isostatic press (HIP) at an elevated temperature above the solution temperature for 718 and conventional AMS 5664 heat treatment under vacuum by NASA MSFC, the latter consisting of 1.25 h ramp from 22 °C to solutioning at 1066 ± 14 °C for ~ 1 h at $1.0\text{-}2.5 \times 10^{-5}$ Torr + air-cool rate-equivalent, followed by 0.88 h ramp from 22 °C to aging at 760 ± 8 °C for 10.0 ± 0.5 h at or below $0.32\text{-}1.1 \times 10^{-5}$ Torr + furnace cool and 649 ± 8 °C hold until 20 h of total aging was reached then furnace cooled. [23].

2.3 Sample preparation and characterization

Samples were extracted from the microstructure-characterization bars for SEM preparation using a Struers Discotom-2 saw. Fig. 1 shows typical images of as-built and heat-treated bars with the orthogonal X, Y, Z directions labeled, that were used to evaluate microstructure in a scanning electron microscope (SEM)



Fig. 1: An example of an (a) as-fabricated metallography bar and (b) a fully heat-treated metallography bar. Z denotes the build direction.

To produce a polished surface for SEM analysis all samples were mounted in Struers PolyFast phenolic resin and planarized with 220 grit SiC paper polish, then polished down with successive steps to 1 μm finish using a Struers Abrapol-2 polisher. This was followed with a 4 – 8-hour final 0.05 μm colloidal silica polish on a vibratory polisher.

Optical microscopy was used to measure average porosity area fraction and grain size. Areas near the edge of each sample were excluded from all analysis since tensile specimens were machined to remove the as-fabricated surface. For porosity measurements, polished surfaces from the X-Z face of each build was imaged employing a 10x objective lens on a Nikon Eclipse MA200 optical microscope using bright field. Five optical images were obtained for each as-built and heat-treated specimen. The locations were reached using an automated stage movement to remove any human bias into the measurements. The pores were then segmented

by contrast using ImageJ where dark defects were assumed to be pores [37]. From the segmented images, area fraction (AF) measurements could be made.

The last microstructure measurements using optical microscopy were grain size of the recrystallized heat-treated samples. Samples were etched with a solution of 85mL H₂O, 45mL HCl, 15mL of HNO₃, and 15mL of HF for 180 seconds using gentle swabbing to highlight the grain boundaries. To calculate the average grain size the ASTM circular intercept procedure E112-13 was used [38]. In this case, three concentric circles were overlaid onto the micrographs of the etched samples using ImageJ processing software version 1.51n and a mark was counted each time a circle intersects a grain boundary. Twin boundaries were excluded from the analysis and over 400 counts were obtained for each powder lot.

A Zeiss Auriga focus ion beam (FIB) SEM utilizing a backscatter electron detector was used at 12 kV to highlight the Nb-rich MC carbides. Electron backscatter diffraction (EBSD) mapping was performed using an EDAX Hikari EBSD detector on the Zeiss Auriga FIB-SEM and a spot size of .75 μm . EBSD data encompassing an area on average of 0.15 mm² per sample was collected using the TSL OIM Data collection 7 software and refined using the TSL OIM Analyzer software. Energy dispersive x-ray spectroscopy (EDS) elemental maps were obtained on a TESCAN MAI3 Triglav SEM with an Oxford X-Max^N silicon drift detector and Aztec version 3.3 software.

2.4 Room temperature tensile tests

Cylindrical tensile samples with a gauge length of 25.4 mm and diameter of 5.1 mm were machined to final dimensions using low stress grinding with final polishing in the gauge section parallel to the longitudinal axis of the sample. Tensile tests were conducted according to ASTM

E8 / E8M - 16ae1 on at least one test bar per build, at room temperature with strain controlled at a strain rate of $3.3 \times 10^{-4} \text{ s}^{-1}$ until 2 % strain using a servo-hydraulic load frame with a capacity of 152 MPa (22k lbf) and extensometer. The control mode of the test was then switched, with stroke controlled to continue at a consistent displacement rate until failure.

2.5 Statistical analysis

Statistical evaluations of responses were performed using Microsoft Excel data analytics toolbox and the JMP® version 11 statistical software package [39]. Variables V were expressed in standardized form V' using equation 2:

$$V' = \frac{(V - V_{\text{mid}})}{0.5 * (V_{\text{max}} - V_{\text{min}})} \quad (2)$$

In equation 2, for each independent variable, V is the actual value measured for a powder lot, V_{max} is the maximum value measured across all powder lots, V_{min} is the minimum value measured across all powder lots, and $V_{\text{mid}} = (V_{\text{max}} + V_{\text{min}})/2$. This produced a range of values from -1 to +1 for each of the independent variables evaluated: Al, Cr, Mo, Nb, Ti, C, N, and O in weight percent. Regression model equations were derived by comparing the results of both forward and reverse stepwise selection of terms, with a 90 % probability of significance required for inclusion of a term. The coefficient of determination with adjustment for number of predictive variables (R^2_{adj}) and the root of the mean of summed squares of remaining errors between the estimated and actual responses (rms error) were used as indications for an equation's goodness of fit. These regressions were intended to objectively screen for significant relationships between composition and grain size then tensile properties, but not to generate the most refined and accurate predictive equations for only estimating optimal compositions.

These expressions using standardized variables V' are useful when comparing these significant relationships, as the relative effect of each significant varied element on the response can be assessed in the derived regression equation by directly comparing the magnitude of the coefficient for each variable [39].

3. Results

3.1 Powder characterization

Below in Table 2 are the quantified powder characteristics (size and circularity) found in this study.

Table 2: Powder size and circularity values

Sample ID	D ₁₀ (um)	D ₅₀ (um)	D ₉₀ (um)	Circularity
1a	17.6	25.13	40.63	0.971
1b	7.54	10.68	23.28	0.984
1c	8.52	20.11	35.16	0.981
2a	7.96	13.35	32.16	0.988
2b	8.25	19.22	41.55	0.971
3a	13.46	23.73	37.93	0.946
3b	12.8	17.9	30.7	0.955
4a	13.92	23	38.56	0.969
4b	10.3	17.7	34.9	0.974
4d	19.77	26.46	39.17	0.936
5a	11.2	14.62	23.82	0.98
5b	17.57	25.27	39.5	0.968
5c	13.8	18.43	29.77	0.941
5d	14.59	23.66	42.36	0.904

From the analysis in Table 2 some notable differences could be observed between the different powder lots even though they were all specified to have ranges between 10 μm and 45 μm from each vendor. Powder lots 1b, 1c, 2a, and 2b were found to have D₁₀ values below the minimum 10 μm diameter range. Powder lot 1b heavily skewed towards finer powder sizes with

90 % of the measured powder particles possessing diameters below 23.28 μm . In contrast no powder lot exhibited a D_{90} value above the 45 μm limit. Lastly, all the powder lots exhibited a circularity value between 0.9 and 1, where powder lot 5d had the lowest value of 0.904 and lot 2a had the highest with 0.988. The differences in circularity did not appear to affect the printability of these powders since each lot adequately flowed during the printing process in this study. It should be noted that powder size and circularity were not measured for lots 3c and 4c.

3.2 Microstructural characterization

The first measurements from the metallography bars were the average porosity AF for both the as-built and fully heat-treated specimen. The results are given in Fig. 2.

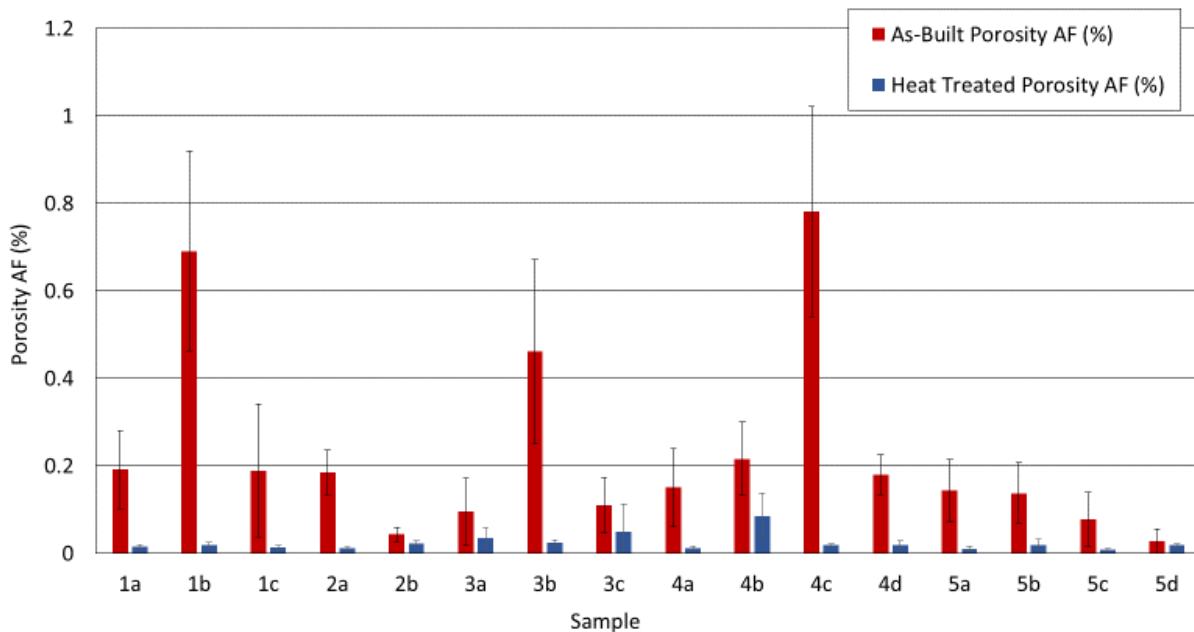


Fig. 2: Average area fraction (AF) porosity measurements for as-built and fully heat-treated specimens.

From the bar charts in Fig. 2, different powder lots presented a range of build qualities despite being created using the same build and treatment parameters. Despite the wide range of measured porosity in the as-built samples, all powder lots resulted in parts with >99.9% densities after undergoing a HIP and heat treatment. This result supports the need for a HIP procedure if a part cannot be fully inspected through nondestructive evaluation (NDE) methods. Micrographs from the build with the largest as-built average porosity AF, 4c, are shown in Fig. 3 in both pre- and post-processing states.

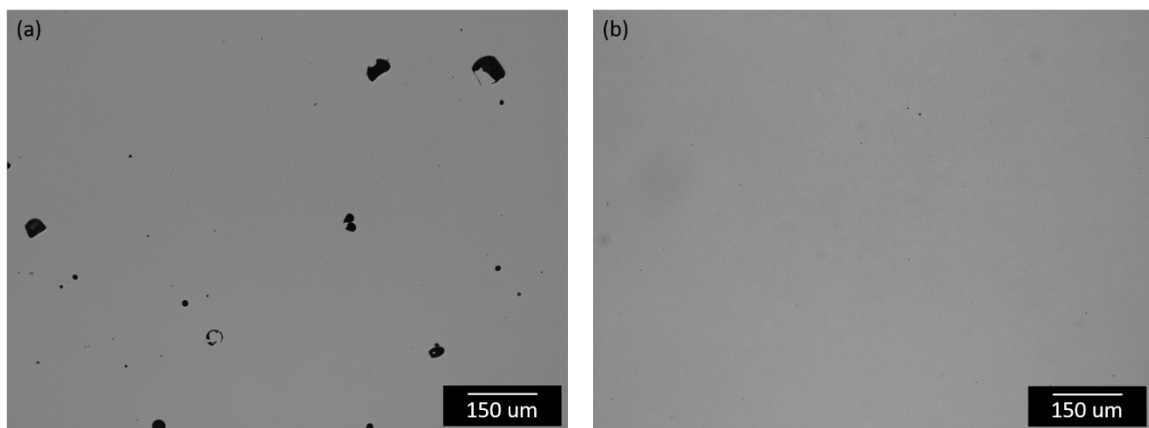


Fig. 3: Representative optical micrographs of sample Alloy 4c in the (a) As-built and (b) fully heat-treated conditions. These images were taken on the XZ-plane parallel to the build direction.

Fig. 3 reveals that interior defects, such as porosity, may be remedied through a HIP post-processing step.

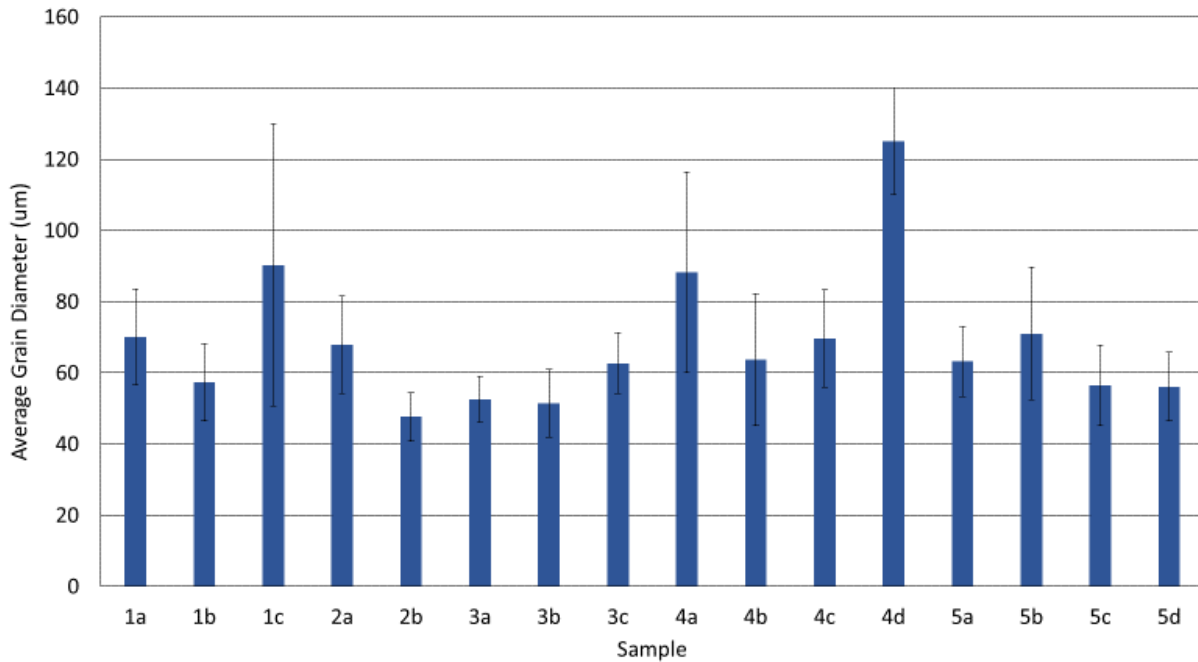


Fig. 4: Average grain diameters for each alloy specimen in the fully heat-treated condition. Error bars represent plus and minus one standard deviation.

Fig. 4 compares the average grain diameter for the various alloys after full heat treatment.

Similar to the as-built porosity measurements, the average grain diameters had large variations between each 718 lot. Indeed, the average measured grain diameter for alloy 2b (48 um) was almost a third of the average diameter measured in 4d (125 um). EBSD grain orientation maps comparing 4d to that of 2b are given in Fig. 5.

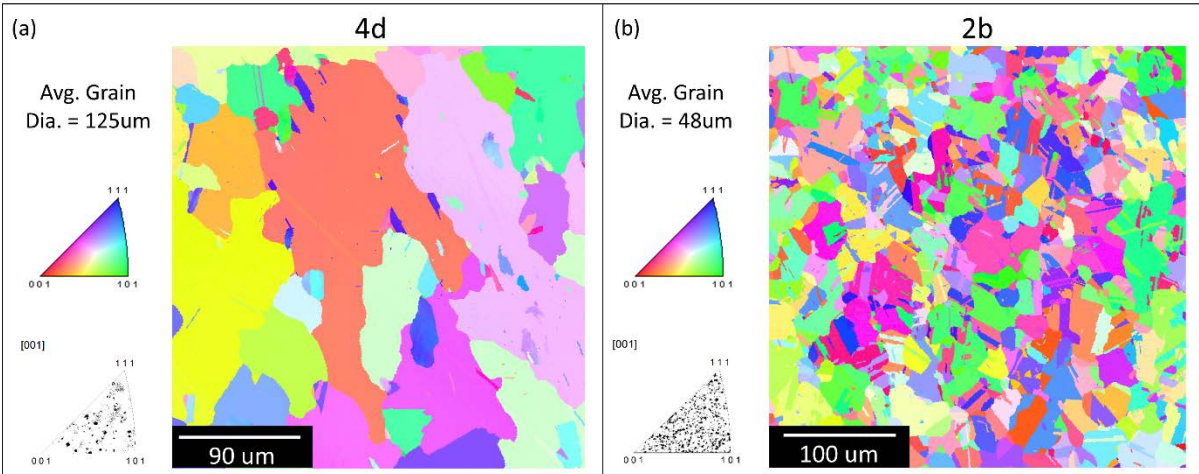


Fig. 5: EBSD maps revealing the striking grain microstructure differences between lots (a) 4d and (b) 2b.

Fig. 5 confirms that even after post-processing significant differences can exist between L-PBF 718 alloys depending on powder characteristics and other yet to be determined factors. To further explore whether other differences existed between the alloys, SEM backscatter images were taken of each fully heat treated 718 alloy sample. Examples of these micrographs are shown in Fig. 6.

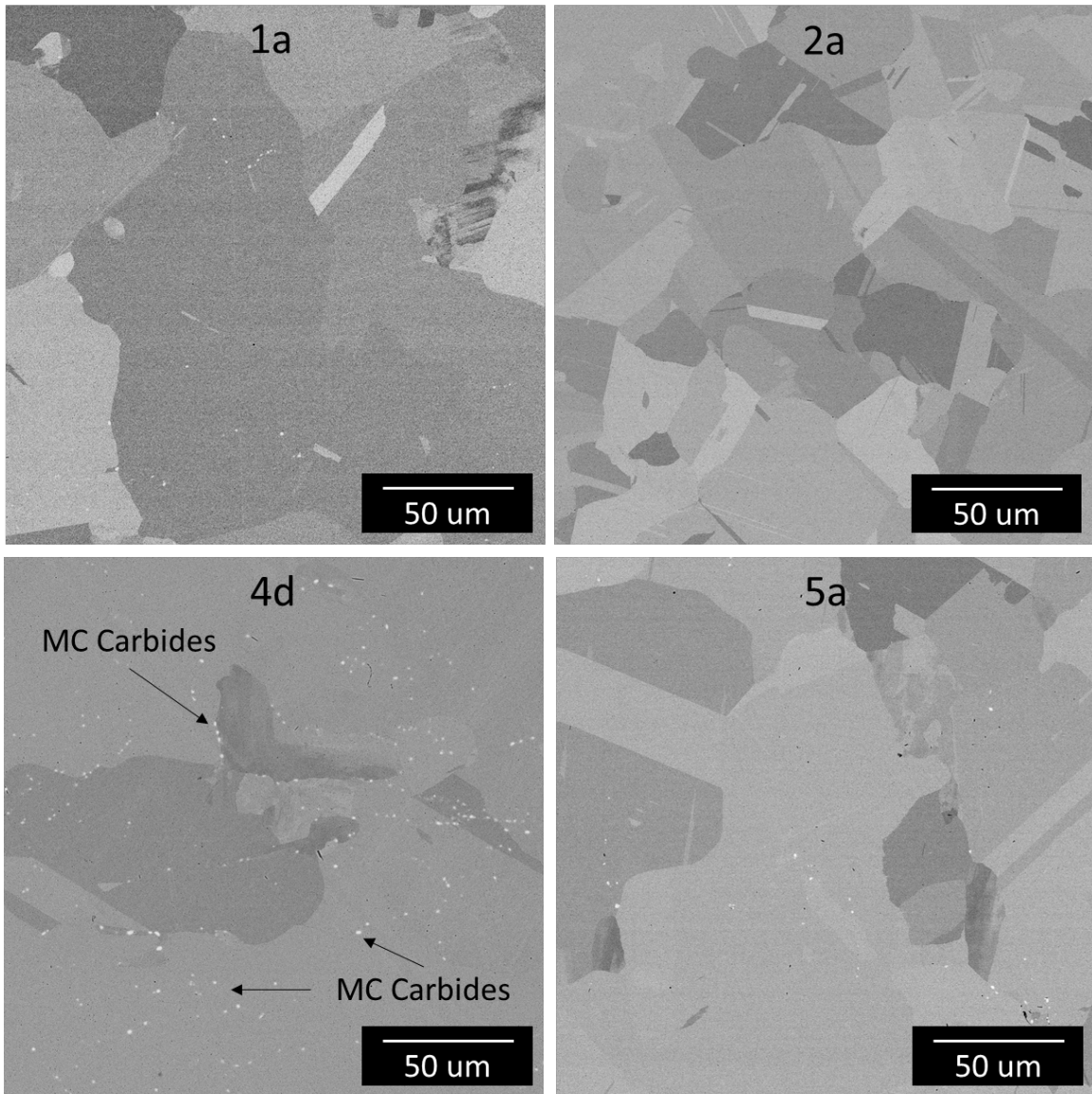


Fig. 6: Representative backscatter SEM images showing microstructures of four different 718 alloys after heat treatment.

Differences in grain size, twin frequency, and secondary carbides (bright phase) can be seen between the four different micrographs shown in Fig. 6. Following the microstructural characterization, tensile properties were evaluated for each 718 build.

3.3 Tensile properties of heat-treated specimens

Room temperature tensile tests were performed on specimens parallel the build direction for each 718 lot. The results for each alloy are given in Table 3.

Table 3: Room temperature tensile properties yield strength (YS), ultimate tensile strength (UTS), and elongation of L-PBF 718 specimen tested along the build direction.

Specimen	YS 0.2% MPa	UTS MPa	Elongation %
1a	1131.3	1354.3	26.8
1b	1133.2	1366.7	26.2
1c	1178.3	1390.8	26.4
2a	1236.0	1439.1	24.1
2b	1234.4	1433.1	26.6
3a	1151.2	1377.1	24.8
3b	1144.8	1370.6	25.8
3c	1150.0	1375.6	26.4
4a	1125.9	1348.8	25.1
4b	1140.3	1362.1	24.9
4c	1141.2	1371.6	26.4
4d	1114.4	1344.0	21.2
5a	1187.1	1401.5	27.3
5b	1185.5	1404.0	25.7
5c	1211.8	1421.7	28.7
5d	1202.2	1405.6	27.6

Values for the 0.2% yield strength (YS), ultimate tensile strength (UTS), and elongation were documented for the 718 alloys. In Table 3, the lowest tensile strength was observed in Build 4d and is highlighted in red. The strongest Build was 2a (highlighted in blue) and the second strongest was from Build 2b. Specimens from Build 4d was tested 20 times to confirm the low strength and ductility values were not an outlier. The averages from these 20 tests is presented in Table 3. Indeed, the variation in yield strength between 2b and 4d was near 120 MPa. This is a significant difference, which likely would also impact the 718 AM part performance at elevated temperatures. The 4d build gave the lowest ductility of 21.2%, the 5c build presented the highest ductility of 28.7%, and most builds had an average ductility about 26%. In Fig. 7

representative stress strain curves from 2a (highest tensile strength), 4d (lowest tensile strength and ductility), and 5c (highest ductility) are presented to highlight the range of tensile properties found within this study.

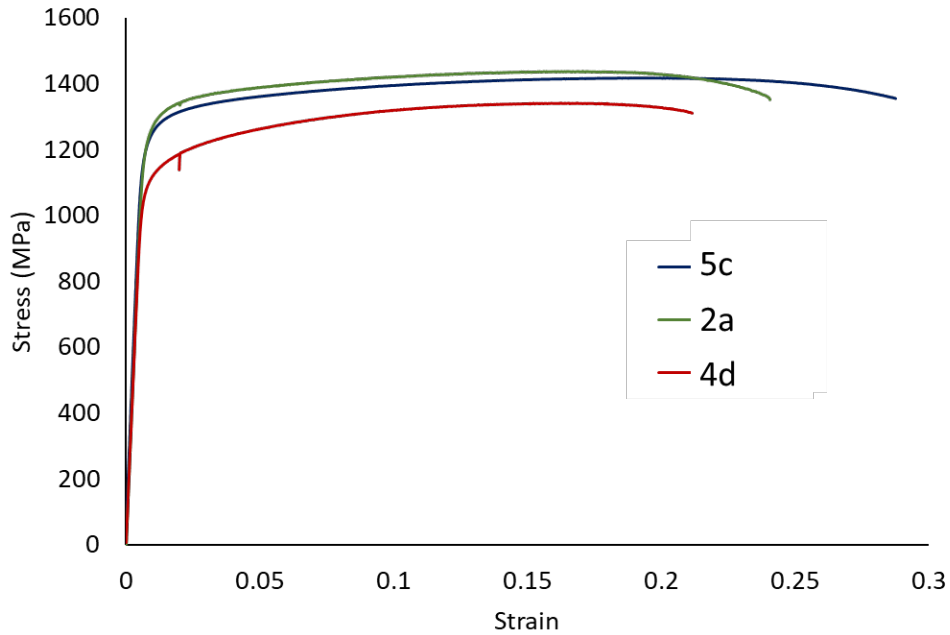


Fig. 7: Stress-strain curves from 2a (highest tensile strength), 4d (lowest tensile strength ductility), and 5c (highest ductility) samples.

Some of these differences can be explain by the microstructural diversity observed in the prior section. Notably, 4d had the largest grain size and the lowest tensile strength consistent with a Hall-Petch trend of grain size versus strength [40]. Despite the same processing parameters and each alloy’s chemistry being within specification, it is noteworthy to observe such large differences in grain size plus porosity, and important to ascertain their origin.

4. Discussion

4.1 Grain size variations – statistical analysis

The grain size differences between the different 718 samples were notable and the cause not well understood. Initially, the HIP process was examined to explore whether heating rate, cooling rate, or sample placement had any bearing on the grain size variations shown in Fig. 4. No differences within the HIP or heat treatment process steps could adequately explain the microstructural differences found in this study. In addition, no correlation existed between the powder sizes (D_{10} , D_{50} , D_{90}) or circularity and grain size that could explain this surprising result.

A one-way analysis of variance in grain size indicated the powder lots of vendor 5 gave significantly larger grain size than the fine grain size observed for powder lots of vendor 4. Powder lots of vendors 1, 2, and 3 gave intermediate grain sizes that did not differ significantly. However, for each vendor this was accompanied by substantial differences in C, Nb, and other elements among their powder lots. As shown in Table 1, the various lots showed differences in composition while falling within AMS 5664 specifications. With these permissible differences, this study is uniquely positioned to statistically explore whether there are correlations between composition and the measured microstructural differences, namely the average measured grain diameter in the fully heat-treated samples. The regression analyses for each element are presented in Table 4.

Table 4: P value correlations between composition and grain size

Element	P Values
Al	0.0237
Cr	0.9727
Fe	0.0024
Mo	0.5031
Nb	0.0002
Ni	0.0450
Ti	0.0041
C	0.0113

N (ppm)	0.6939
O (ppm)	0.0424

From Table 4, multiple elements are found to be significantly correlated to the grain size when using 0.05 as a critical p-value threshold. Though, Nb presented the strongest correlation. Below is a scatter plot of the Nb content (wt.%) versus measured grain size given in Fig. 4 to highlight the relationship.

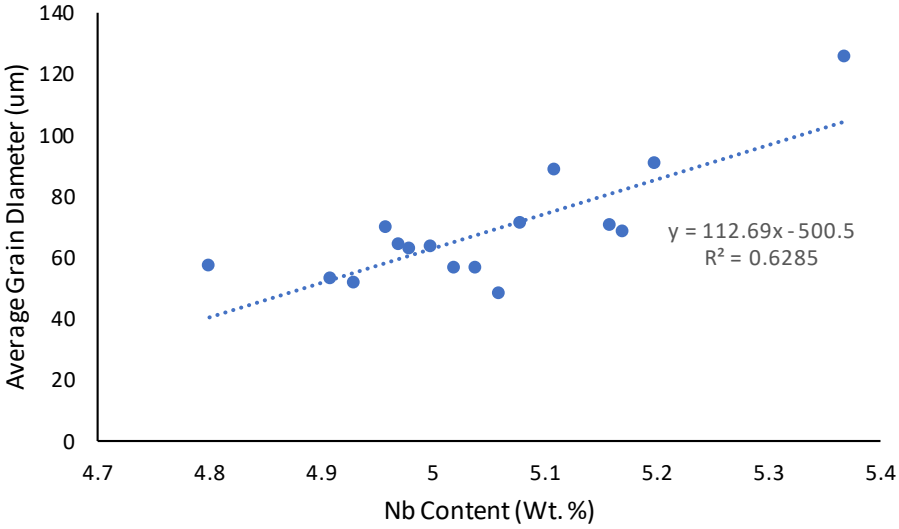


Fig. 8: Relationship between Niobium content and average grain diameter of the 718 builds.

Despite the strong correlation between Nb content and grain size shown in Fig. 8, other elements also appeared to be correlated as shown in table 4 making it difficult to discern which elements primarily influenced the AM 718 average grain size from this analysis alone. Therefore, the relationship of grain size with alloy composition was assessed using stepwise linear regression as described in the Experimental section, with elements Al, Cr, Mo, Nb, Ti, C, N, and O in weight percent standardized according to equation (2) to ascertain a significant

relationship between composition and grain size. This evaluation yielded the linear regression relationship:

$$\text{Grain Size } (\mu\text{m}) = 73.7 + 27.6 \text{ Nb}' + 17.9 \text{ C}' \quad (3)$$

with an adjusted coefficient of determination $R^2_{\text{adj}} = 0.78$ and rms error = 9.0 μm . This relationship indicated that Nb content had the strongest positive influence on grain size, followed by C. Interestingly, these elements contribute to the formation of Nb-rich MC carbides [41,42]. This trend appears to be supported by Fig. 6 which revealed a large amount of carbides in 4d, which also had the largest grain size. To confirm this trend, EDS analysis of these secondary phases was performed and are shown in Fig. 9.

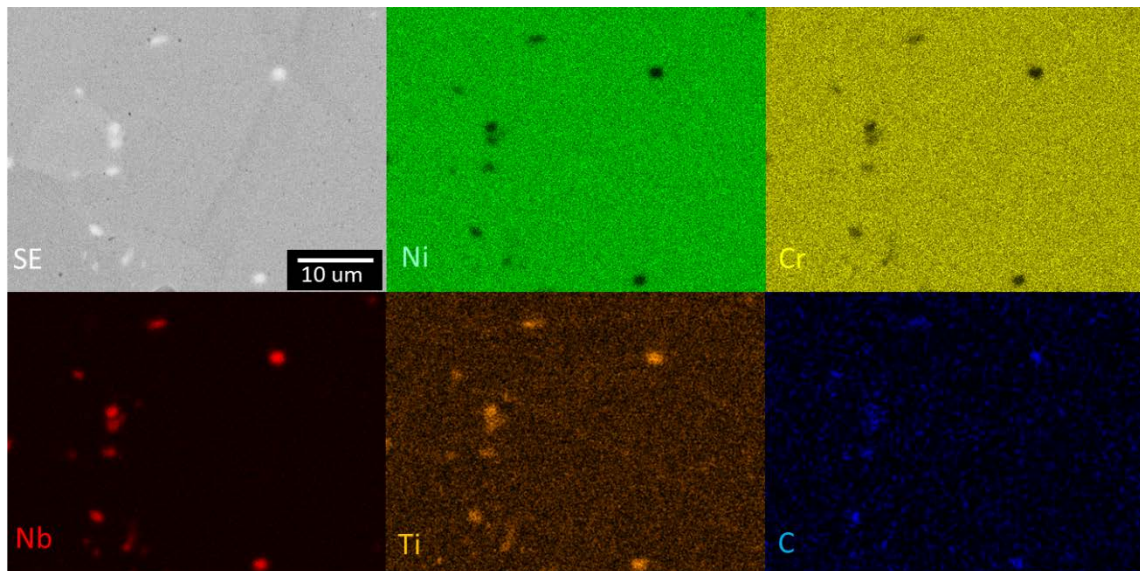


Fig. 9: EDS chemical maps revealing Ti and Nb-rich MC carbides in the 4d alloy.

Fig. 9 confirms that 4d has a large amount of Nb and Ti-rich MC carbides throughout its microstructure. In fact, a qualitative assessment of Fig. 6 suggests that build 4d had the highest

volume fraction of carbides found in this study as well as the highest C content and largest grain size. The carbide volume fraction combined with Equation 3 suggests that having higher amounts of carbon and niobium may drive intragranular MC carbide formation and may cause significant grain growth during the post-processing steps of the 718 alloy. Typically, higher levels of Nb promote δ phase formation and higher strength. The reduced strength of build 4d may be explained by the larger amount of MC carbides removing free Nb from the microstructure and thus inhibiting δ phase formation. This theory is supported by the relatively larger amounts of grain boundary δ phase found in alloys 2a and 2b that were not present in 4d as shown in Fig. 10.

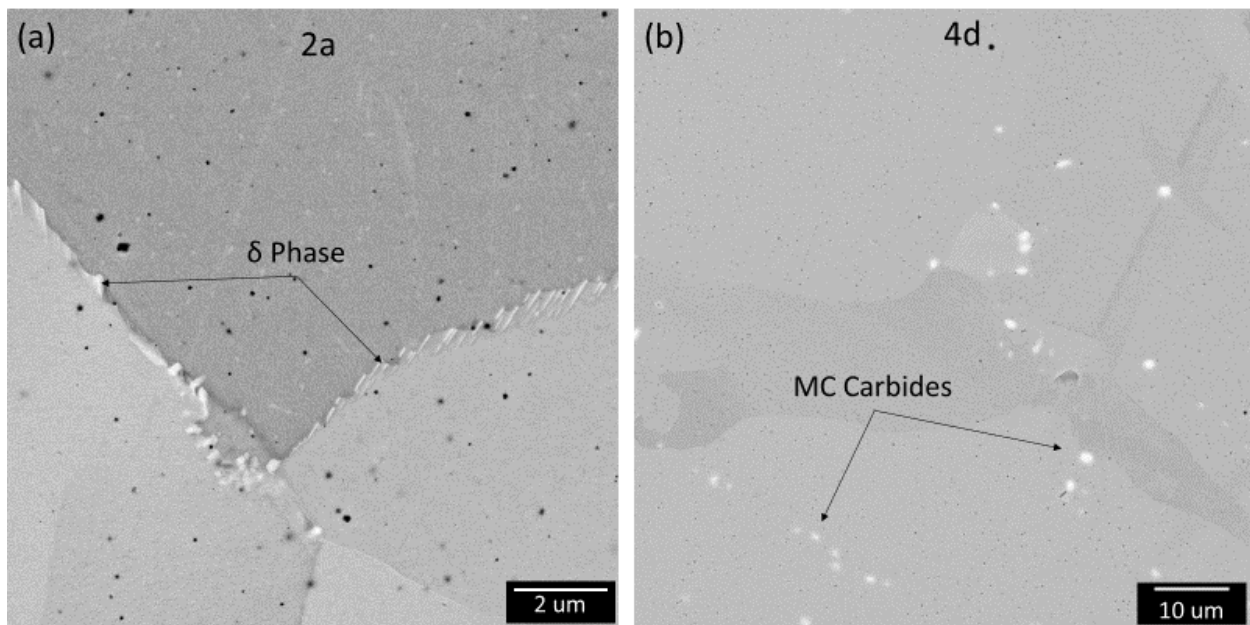


Fig. 10: SEM backscatter images of Alloy (a) 2a and (b) 4d.

As shown in Fig. 10, lot 2a has a notable amount of the needle-like $\text{Ni}_3\text{Nb DO}_a$ δ phase along its grain boundaries while 4d is dominated by Nb and Ti-rich intragranular MC carbides that rarely lie along grain boundaries. These needle-like precipitates were confirmed to be the δ phase through EDS analysis which revealed higher amounts of Ni and Nb. As the MC carbides have a higher solvus temperature than δ phase (1300°C vs. 1040°C, respectively), their presence may hinder δ phase formation by sequestering free Nb to form carbides instead [22]. In fact, a recent study by Zhao et al. [43] found a correlation between Nb homogeneity and the formation of NbC carbides which consequentially influenced grain growth kinetics during heat treatments. A similar trend was also found by Wei *et al.* who found that higher amounts of carbon suppressed the formation of eutectic γ' in a polycrystalline Ni-base superalloy by removing available Ti [44]. By suppressing δ phase, grain size differences caused by post processing would be expected. δ phase is known for controlling grain growth during 718 heat treatments [45]. This grain growth control is even more important in AM 718, which may undergo additional high temperature stress relief and HIP processing steps to remove residual stress, defects, and texture, processes not employed for wrought alloys [28]. Furthermore, the small dark precipitates seen in both alloys in Fig. 10 were confirmed to be TiN's through EDS which found elevated amounts of Ti and N associated with the particles. These nanoscale nitrides were observed in every AM 718 build despite having been atomized in argon rather than nitrogen. A recent study found that if the number of nitrides exceeded some yet to be determined critical amount then the as-built anisotropic grain texture would be pinned preventing recrystallization [34]. This suggests that both nitrogen and carbon need to be well controlled in 718 powder lots intended for AM to control grain size and texture.

4.2 Tensile strength variations –statistical analysis

Grain size was not the only measured property that revealed surprising differences between the different samples, yield strength and tensile strength both varied significantly from build to build. Again, no correlation between the powder characteristics and mechanical properties was found to explain this difference. Interestingly, the measured grain size differences could not fully explain the observed mechanical property differences as no significant correlation was found between grain size and yield strength ($p=0.09$) or grain size and tensile strength ($p=.067$). Instead, a one-way analysis of variance in yield strength and ultimate strength indicated the powder lots of vendors 2 and 5 gave significantly higher strengths than those of the vendors 3, 1, and 4. However, for each vendor this was again accompanied by substantial differences in all the elements among their powder lots. The statistically significant correlations between composition and two key tensile properties, 0.2% yield strength (YS) and ultimate tensile strength (UTS), were also examined with linear regression using a critical threshold p value of 0.05 as shown in Table 5.

Table 5: P value correlations between composition and yield (YS) and ultimate tensile (UTS) strength

Element	P Value - YS	P Value - UTS
Al	0.5468	0.3884
Cr	0.5859	0.5507
Fe	0.4044	0.2963
Mo	0.7358	0.6020
Nb	0.8421	0.9537
Ni	0.3715	0.2803
Ti	0.8073	0.6542
C	0.0012	0.0014
N (ppm)	0.0994	0.0822
O (ppm)	0.4454	0.3570

In contrast to the results for grain size, only one alloying element (C) appears to have a significant correlation to the tensile properties. Scatter plots of C content (wt.%) versus measured yield and tensile strengths are given in Fig. 11.

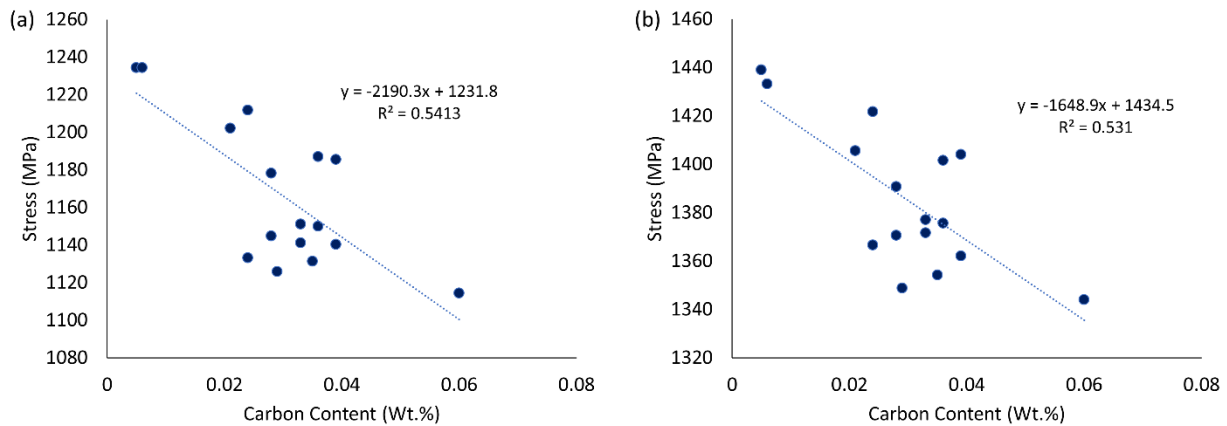


Fig. 11: (a) carbon content vs yield strength and (b) carbon content vs tensile strength.

Clear trends between C content and the measured tensile properties are observed in Fig. 11, where higher amounts of carbon resulted in reduced tensile strengths. Indeed, even when 4d, the alloy with the lowest strength and highest C content is removed a statistically significant correlation between C content and strength still exists ($p=0.0036$ for yield strength and $p=0.005$ for tensile strength). Still, more robust analyses between the relationships of yield strength and ultimate tensile strength with alloy composition was performed using stepwise linear regression as described in the Experimental section, with elements in weight percent standardized according to equation (2).

Conventional linear regressions were performed using the baseline results from one tensile tested specimen of each powder lot. In this approach assuming each response is normally distributed around the mean, one can pool the residual error between the response value

estimated by the regression and the actual value in order to estimate remaining random deviations of each response, reported here as the root mean square (rms) error. This parameter is often used to help assess the significance of reported and estimated values and trends. The remaining degrees of freedom for estimating rms error was 11 for each regression equation, sufficient for reasonable estimates of the rms error. The results of 20 subsequent tensile tests performed on powder lot 4d were later used to help assess these assumptions. The assumption of normal distribution was confirmed to be applicable for the responses of yield strength, ultimate strength, elongation, and reduction in area. The standard deviations were estimated for each of these responses, using the 20 tensile tests performed for this one powder lot. This gave a standard deviation of 7.9 MPa for yield strength, 8.9 MPa for ultimate strength, and 1.0 % for elongation. As shown in Fig. 11, the differences in yield strength and ultimate strengths across different powder lots were found to be over ten times their standard deviations. The rms error of each regression equation presented below was significantly larger than the standard deviation of the associated response in the 20 tests. This confirmed that the regression equations and rms error terms were reasonable, yet not “over-fitting” the data. There could be concerns that tensile response varied systematically rather than randomly as a function of location across the build plate. Interestingly, the results of the single initial test for 4d were in fact quite close to mean values derived from the 20 subsequent tests. This suggested that the consistent specimen/location on each build plate selected for the single initial tensile test was sufficiently representative of response for the specimens on a build plate, for the present purposes.

This yielded the linear regression relationships:

$$\text{Yield Strength (MPa)} = 1167.8 + 32.4 Al' + 20.7 Cr' + 52.9 Ti' - 85.7 C' \quad (4)$$

with an adjusted coefficient of determination $R^2_{\text{adj}} = 0.77$ and rms error = 18.7 MPa.

$$\text{Ultimate Tensile Strength (MPa)} = 1387.5 + 27.9 Al' + 16.0 Cr' + 37.6 Ti' - 62.7 C' \quad (5)$$

with an adjusted coefficient of determination $R^2_{\text{adj}} = 0.73$ and rms error = 15.3 MPa. These

similar relationships indicated that increasing Ti had the strongest positive influence on strength, followed by Al and then Cr. Al and Ti likely are associated positively with strength as they primarily contribute to the formation of the strengthening γ' phase in 718 [32]. However, C had an even stronger negative influence on strength.

As shown from the predictive expressions for both yield strength and tensile strength as well as the trend lines shown in Fig. 11, carbon was the only element negatively correlated to strength. One reason that may describe this result was discussed in the previous section. Higher amounts of carbide formers appear to suppress the formation of δ phase, thereby leading to uncontrolled grain growth during post-processing. Polycrystalline alloys with larger grain sizes will have reduced tensile properties—especially at room temperature [40]. Still, as stated previously grain size could not fully explain the tensile strength differences between builds. Another possible cause of this effect again may be due to the formation of the Ti and Nb-rich MC carbides. Both Ti and Nb are important alloying elements for the formation of the strengthening γ' ($\text{Ni}_3\text{Al,Ti}$) and γ'' (Ni_3Nb) phases, respectively [46–48]. Already, some amount of Ti was consumed to form detrimental nitrides in these alloys [34]. Therefore, as the MC carbide formation was increased, even less Ti and Nb would be available for the formation of these crucial strengthening phases. In addition, precipitate free denuded zones may occur near the carbides. This combination of larger overall grain size and fewer strengthening precipitates

would be expected to result in AM 718 builds with reduced tensile strength and may explain the differences in strength found in this study.

4.3 Thermodynamic simulations

In sections 4.1 and 4.2, it was found that carbon amounts may play a role in suppressing both the grain controlling δ phase and the strengthening γ' and γ'' phases. To explore this relationship, thermodynamic phase simulations were performed to investigate the effect carbon levels in 718 may have on the phase stability and formation of important intermetallic precipitates, such as δ phase. Thermodynamic simulations were completed using the ThermoCalc database for Nickel-based alloys, TCNI9, with the unobserved σ phase manually turned off. Fig. 12 shows two diagrams where the stable equilibrium phases are shown at each temperature. The top fig. corresponds to the average composition of Inconel 718 chemistries in this work, with C content set to 0.02975 wt.%, and N and O content set to zero. The bottom fig. corresponds to the same average chemistry but with 0.06 wt.% C, representing the maximum amount found in the study.

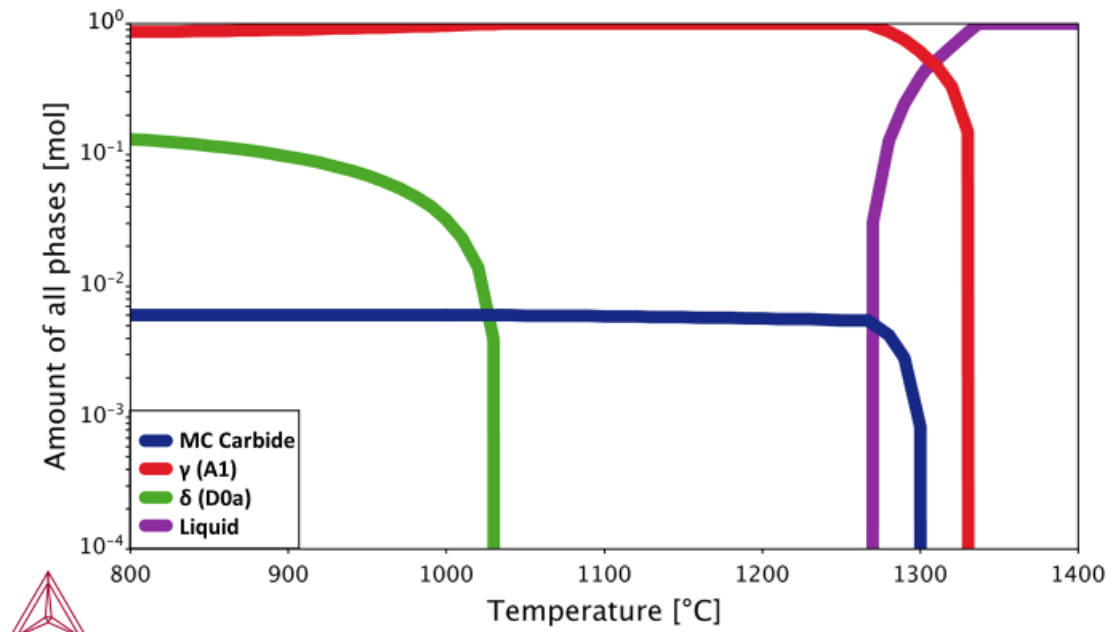
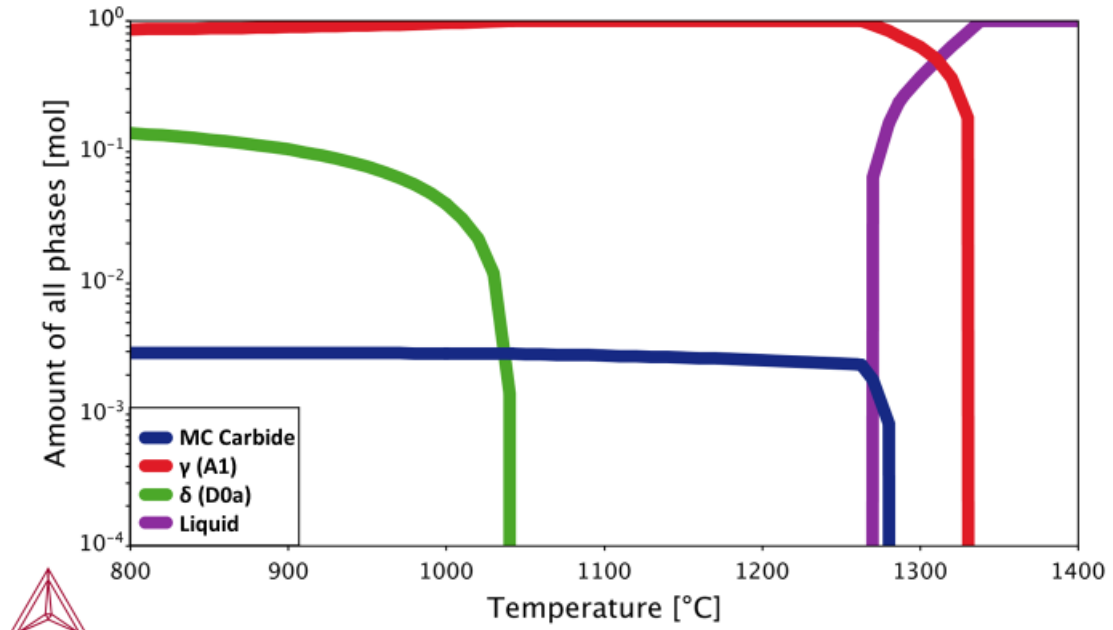


Fig. 12: Phase diagram plots comparing the molar volume fractions of stable phases in representative 718 compositions with 0.02975 wt.% C (top), and 0.06 wt.% C (bottom).

The plots show the same phases in both: liquid, γ matrix (A1), the MC carbides, and δ phase (D0a). Two notable differences are the δ solvus, and MC carbide amount and solvus. To examine this in further detail, these values were tracked with a few additional simulations.

Fig. 13 reveals the volume fraction and solvus temperatures for MC carbides and the δ phase with respect to carbon concentrations. In Fig. 13(a) and 13(b), the δ phase solvus temperature and volume fraction decrease notably over the range of C tested, while the MC carbide solvus temperature and volume fraction increase as shown in Fig. 13(c) and 13(d). The volume fractions were calculated at 900°C which is the lower temperature bound of the grain growth range for nickel [49] and the approximate temperature where the maximum rate of δ phase precipitate occurs in 718 [45].

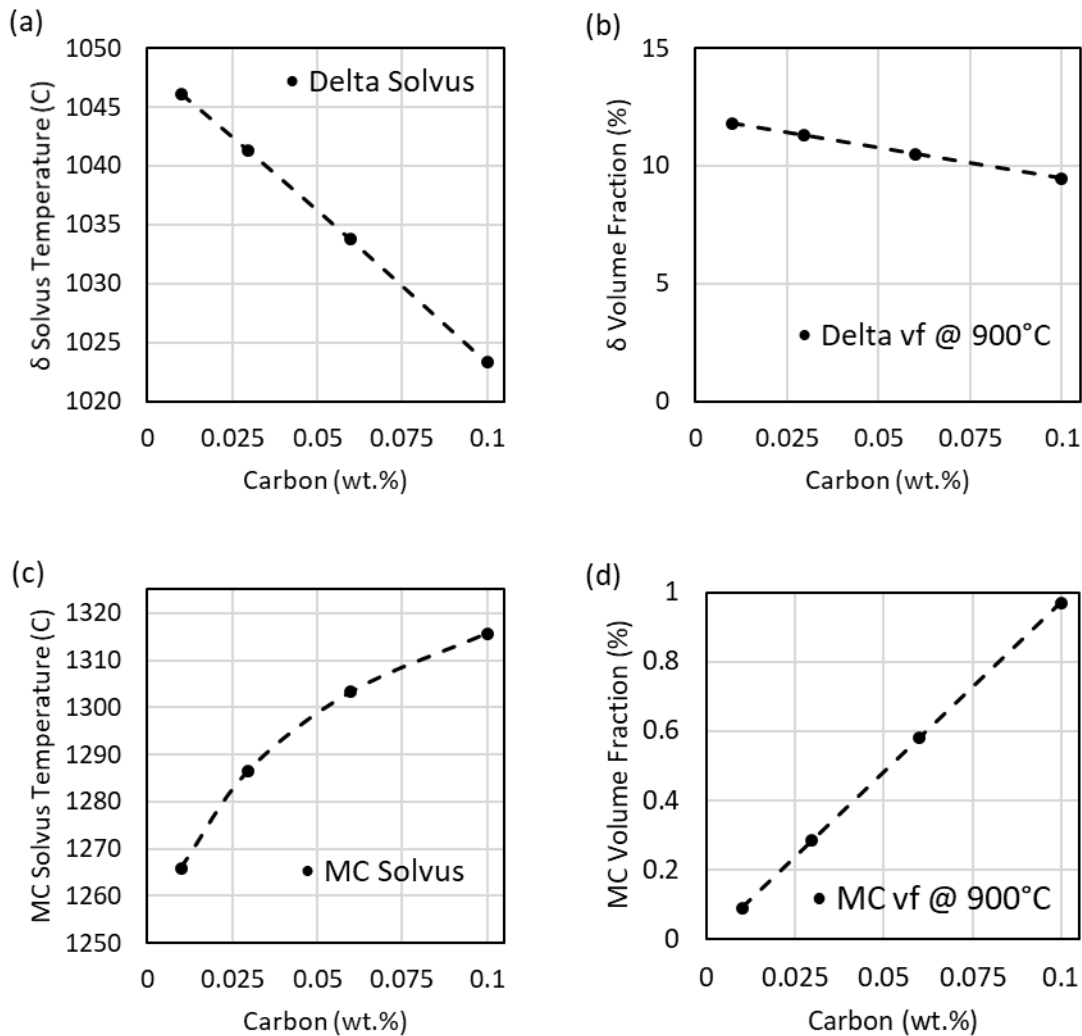


Fig. 13: Plots showing the a) δ solvus, b) δ volume fraction (vf) at 900°C, c) MC carbide solvus, and d) MC carbide volume fraction (vf) as a function of C content at 900°C.

The thermodynamic calculations support the experimental observations described in the study.

As carbon increases, so does the formation and frequency of MC carbides at the detriment of the grain boundary stabilizing δ phase and likely the strengthening γ' and γ'' phases. Another notable observation is the reduction of the δ phase solvus temperature. This may explain some of the grain size differences observed in the AM 718 alloys. By suppressing the δ phase solvus, grains can grow for longer periods of time during the multiple post processing steps. AM 718

alloys will be even more sensitive to this decrease in the δ phase solvus temperature as the added HIP step typically has a notably slow cooling rate ($2^{\circ}\text{C}/\text{min}$). Therefore, AM 718 alloy's which have high C amounts will need to be processed differently than those with lower C amounts as the δ phase in each will not behave the same. This is further confirmed by the lack and abundance of δ phase observed between Alloys 4d and 2a, respectively (Fig. 10). The combined experimental and computational results highlight the need for refined compositional guidelines in alloys that will be processed through AM. In the case of AM 718, the allowable amount of carbon needs to be reassessed along with the corresponding heat treatment guidelines.

5. Conclusions

In this study, 16 different 718 powder lots were processed using L-PBF with the same build and post-processing parameters. From the microstructure and mechanical analysis significant findings were made as listed below.

- 1.) All 718 powder lots/alloys yielded fully dense L-PBF builds ($>99.9\%$ density) after HIP.
- 2.) Despite each 718 alloy being built using the same laser and post processing parameters, observable microstructural differences, including grain size ($48\ \mu\text{m}$ to $125\ \mu\text{m}$), MC carbide frequency, and δ phase formation were found.
- 3.) The measured differences in grain diameter were likely caused by an excess of MC carbides, which consequentially suppressed the formation of intergranular δ phase and allowed uncontrolled grain growth during post processing.

- 4.) Higher amounts of Nb-rich MC carbides combined with the presences of Ti-rich nitrides likely limited the strengthening γ' and γ'' phase development and lead to compromised strength of those AM 718 builds.
- 5.) Thermodynamic simulations revealed that higher carbon content will result in a lower nucleation frequency and solvus/formation temperature of grain growth-controlling δ phase.
- 6.) Permissible level of carbon may need to be further considered in 718 powder lots which will be utilized in AM.

From these results, the authors recommend a larger study be performed to determine a refined chemical standard for more consistent performance of AM 718. Finally, these conclusions highlight the important opportunity to refine new composition standards and resulting performance for other alloys that are to be adapted through the emerging, and promising additive manufacturing route.

Acknowledgements

TMS would like to acknowledge the NASA Human Exploration and Operations Mission Directorate (HEOMD) Space Launch System Liquid Engine Office Project for funding this study under the Additive Manufacturing Structural Integrity Initiative project. TMS also acknowledges Dereck Johnson (NASA-GRC) for his help with the chemistry measurements.

Data Availability

The data that support the findings of this study are available from the corresponding author on reasonable request.

References

- [1] K. Amato, S.M. Gaytan, L. Murr, E. Martinez, P. Shindo, J. Hernandez, S. Collins, F. Medina, Microstructure and mechanical behavior of Inconel 718 fabricated by selective laser melting, *Acta Mater.* 60 (2012) 2229–2239.
- [2] A. Strondl, M. Palm, J. Gnauk, G. Frommeyer, Microstructure and mechanical properties of nickel based superalloy IN718 produced by rapid prototyping with electron beam melting (EBM), *Mater. Sci. Technol.* 27 (2011) 876–883.
- [3] L. Parimi, G.A. Ravi, D. Clark, M.M. Attallah, Microstructural and texture development in direct laser fabricated IN718, *Mater. Charact.* 89 (2014) 102–111.
- [4] K. Wang, Y. Liu, Z. Sun, J. Lin, Y. Lv, B. Xu, Microstructural evolution and mechanical properties of Inconel 718 superalloy thin wall fabricated by pulsed plasma arc additive manufacturing, *J. Alloys Compd.* 819 (2020) 152936.
<https://doi.org/10.1016/j.jallcom.2019.152936>.
- [5] J.H. Yi, J.W. Kang, T.J. Wang, X. Wang, Y.Y. Hu, T. Feng, Y.L. Feng, P.Y. Wu, Effect of laser energy density on the microstructure, mechanical properties, and deformation of Inconel 718 samples fabricated by selective laser melting, *J. Alloys Compd.* 786 (2019) 481–488.
<https://doi.org/10.1016/j.jallcom.2019.01.377>.
- [6] A. Lingenfelter, Welding of Inconel Alloy 718: A Historical Overview, *Superalloy 718 - Metall. Appl.* (1989) 673–683. https://doi.org/10.7449/1989/superalloys_1989_673_683.
- [7] M. Smith, L. Bichler, J. Gholipour, P. Wanjara, Mechanical properties and microstructural

- evolution of in-service Inconel 718 superalloy repaired by linear friction welding, *Int. J. Adv. Manuf. Technol.* 90 (2017) 1931–1946. <https://doi.org/10.1007/s00170-016-9515-2>.
- [8] M. Godec, S. Malej, D. Feizpour, Donik, M. Balažic, D. Klobčar, L. Pambaguian, M. Conradi, A. Kocijan, Hybrid additive manufacturing of Inconel 718 for future space applications, *Mater. Charact.* 172 (2021).
<https://doi.org/10.1016/j.matchar.2020.110842>.
- [9] C. Zhao, K. Fezzaa, R.W. Cunningham, H. Wen, F. De Carlo, L. Chen, A.D. Rollett, T. Sun, Real-time monitoring of laser powder bed fusion process using high-speed X-ray imaging and diffraction, *Sci. Reprts.* 7 (2017) 1–11. <https://doi.org/10.1038/s41598-017-03761-2>.
- [10] P. Bidare, I. Bitharas, R.M. Ward, M.M. Attallah, A.J. Moore, Fluid and particle dynamics in laser powder bed fusion, *Acta Mater.* 142 (2018) 107–120.
<https://doi.org/10.1016/j.actamat.2017.09.051>.
- [11] B. Zhang, Y. Li, Q. Bai, Defect Formation Mechanisms in Selective Laser Melting: A Review, *Chinese J. Mech. Eng. (English Ed.)* 30 (2017) 515–527.
<https://doi.org/10.1007/s10033-017-0121-5>.
- [12] E. Chlebus, K. Gruber, B. Ku, J. Kurzac, T. Kurzynowski, *Materials Science & Engineering A* Effect of heat treatment on the microstructure and mechanical properties of Inconel 718 processed by selective laser melting, 639 (2015) 647–655.
<https://doi.org/10.1016/j.msea.2015.05.035>.
- [13] T. Trosch, J. Strößner, R. Völkl, U. Glatzel, Microstructure and mechanical properties of

- selective laser melted Inconel 718 compared to forging and casting, *Mater. Lett.* 164 (2016) 428–431. <https://doi.org/10.1016/j.matlet.2015.10.136>.
- [14] G.A. Rao, M. Kumar, M. Srinivas, D.S. Sarma, Effect of standard heat treatment on the microstructure and mechanical properties of hot isostatically pressed superalloy inconel 718, *Mater. Sci. Eng. A.* 355 (2003) 114–125. [https://doi.org/10.1016/S0921-5093\(03\)00079-0](https://doi.org/10.1016/S0921-5093(03)00079-0).
- [15] Y.J. Kang, S. Yang, Y.K. Kim, B. AlMangour, K.A. Lee, Effect of post-treatment on the microstructure and high-temperature oxidation behaviour of additively manufactured inconel 718 alloy, *Corros. Sci.* 158 (2019) 108082. <https://doi.org/10.1016/j.corsci.2019.06.030>.
- [16] K. Solberg, F. Berto, What is going on with fatigue of additively manufactured metals?, *Mater. Des. Process. Commun.* 1 (2019) 21–24. <https://doi.org/10.1002/mdp2.84>.
- [17] K. Solberg, D. Wan, F. Berto, Fatigue assessment of as-built and heat-treated Inconel 718 specimens produced by additive manufacturing including notch effects, *Fatigue Fract. Eng. Mater. Struct.* 43 (2020) 2326–2336. <https://doi.org/10.1111/ffe.13300>.
- [18] NASA, MSFC-STD-3716 - Standard for Additively Manufactured Spaceflight Hardware By Laser Powder Bed Fusion, (2017) 93. <https://doi.org/MSFC-STD-3716>.
- [19] NASA, MSFC-SPEC-3717 - Specification for Control and Qualification of Laser Powder Bed Fusion Metallurgical Processes, (2017) 58. <https://doi.org/MSFC-SPEC-3717>.
- [20] Q. Han, R. Mertens, M.L. Montero-Sistiaga, S. Yang, R. Setchi, K. Vanmeensel, B. Van

- Hooreweder, S.L. Evans, H. Fan, Laser powder bed fusion of Hastelloy X: Effects of hot isostatic pressing and the hot cracking mechanism, *Mater. Sci. Eng. A.* 732 (2018) 228–239. <https://doi.org/10.1016/j.msea.2018.07.008>.
- [21] W.E. Frazier, Metal Additive Manufacturing : A Review, *J. Mater. Eng. Perform.* 23 (2014) 1917–1928. <https://doi.org/10.1007/s11665-014-0958-z>.
- [22] R. Jiang, A. Mostafaei, J. Pauza, C. Kantzos, A.D. Rollett, Varied heat treatments and properties of laser powder bed printed Inconel 718, *Mater. Sci. Eng. A.* 755 (2019) 170–180. <https://doi.org/10.1016/j.msea.2019.03.103>.
- [23] SAE, AMS5664F, 2017. <https://www.sae.org/standards/content/ams5662m/>.
- [24] G.A. Rao, M. Srinivas, D.S. Sarma, Effect of oxygen content of powder on microstructure and mechanical properties of hot isostatically pressed superalloy Inconel 718, *Mater. Sci. Eng. A.* 435–436 (2006) 84–99. <https://doi.org/10.1016/j.msea.2006.07.053>.
- [25] J. Schneider, B. Lund, M. Fullen, Effect of heat treatment variations on the mechanical properties of Inconel 718 selective laser melted specimens, *Addit. Manuf.* 21 (2018) 248–254. <https://doi.org/10.1016/j.addma.2018.03.005>.
- [26] L. Huang, Y. Cao, J. Zhang, X. Gao, G. Li, Y. Wang, Effect of heat treatment on the microstructure evolution and mechanical behaviour of a selective laser melted Inconel 718 alloy, *J. Alloys Compd.* 865 (2021) 158613. <https://doi.org/10.1016/j.jallcom.2021.158613>.
- [27] E. Hovig, O. Berg, T. Aukrust, H. Solhaug, Effect of Heat Treatment on the Ductility of

- Inconel 718 Processed by Laser Powder Bed Fusion, *Adv. Autom. Manuf.* IX. (2020) 98–105.
- [28] E. Hosseini, V.A. Popovich, A review of mechanical properties of additively manufactured Inconel 718, *Addit. Manuf.* 30 (2019).
- [29] M. Ni, C. Chen, X. Wang, P. Wang, R. Li, X. Zhang, K. Zhou, Anisotropic tensile behavior of in situ precipitation strengthened Inconel 718 fabricated by additive manufacturing, *Mater. Sci. Eng. A.* 701 (2017) 344–351. <https://doi.org/10.1016/j.msea.2017.06.098>.
- [30] W.M. Tucho, P. Cuvillier, A. Sjolyst-Kverneland, V. Hansen, Microstructure and hardness studies of Inconel 718 manufactured by selective laser melting before and after solution heat treatment, *Mater. Sci. Eng. A.* 689 (2017) 220–232. <https://doi.org/10.1016/j.msea.2017.02.062>.
- [31] V.A. Popovich, E. V. Borisov, A.A. Popovich, V.S. Sufiiarov, D. V. Masaylo, L. Alzina, Impact of heat treatment on mechanical behaviour of Inconel 718 processed with tailored microstructure by selective laser melting, *Mater. Des.* 131 (2017) 12–22. <https://doi.org/10.1016/j.matdes.2017.05.065>.
- [32] E. Chlebus, K. Gruber, B. Kuźnicka, J. Kurzac, T. Kurzynowski, Effect of heat treatment on the microstructure and mechanical properties of Inconel 718 processed by selective laser melting, *Mater. Sci. Eng. A.* 639 (2015) 647–655. <https://doi.org/10.1016/j.msea.2015.05.035>.
- [33] T. Smith, N. Derimow, C. Kantzos, T. Leibengood, A. Thompson, T. Gabb, High

- Temperature Properties of Dispersion Strengthened Medium-Entropy Alloys Produced by Additive Manufacturing, JANNAF J. Propuls. Energ. submitted (2020).
- [34] C.K. Sudbrack, B.A. Lerch, T.M. Smith, I.E. Locci, D.L. Ellis, A.C. Thompson, B. Richards, Impact of powder Variability on the Microstructure and mechanical Behavior of Selective Laser Melted 718, Proc. 9th Int. Symp. Superalloy 718 Deriv. Energy, Aerospace, Ind. Appl. (2018) 89–113.
- [35] H. Yang, L. Meng, S. Luo, Z. Wang, Microstructural evolution and mechanical performances of selective laser melting Inconel 718 from low to high laser power, J. Alloys Compd. 828 (2020) 154473. <https://doi.org/10.1016/j.jallcom.2020.154473>.
- [36] Z. Yunhao, K. Li, M. Gargani, W. Xiong, A comparative analysis of Inconel 718 made by additive manufacturing and suction casting: Microstructure evolution in homogenization, Addit. Manuf. 36 (2020).
- [37] M.D. Abramoff, P.J. Magalhaes, S.. Ram, Image Processing with ImageJ, Biophotonics Int. 11 (2004) 36–44.
- [38] ASTM, Standard Test Methods for Determining Average Grain Size, 2013.
- [39] B. Jones, J. Sall, JMP Statistical Discovery Software, (2011) 188–194.
- [40] D.J. Dunstan, A.J. Bushby, Grain size dependence of the strength of metals: The Hall-Petch effect does not scale as the inverse square root of grain size, Int. J. Plast. 53 (2014) 56–65. <https://doi.org/10.1016/j.ijplas.2013.07.004>.
- [41] J.P. Collier, S.H.O.W. Wong, J.C. Phillips, J.K. Tien, The Effect of Varying Al , Ti , and Nb

- Content on the Phase Stability of INCONEL 718, *Metall. Trans. A.* 19 (1988) 1657–1666.
- [42] L. Wenchang, X. Furen, Y. Mei, C. Zonglin, W. Shaogang, L. Weihong, Quantitative Phase Analysis of Inconel 718 by X-ray Diffraction, *J. Mater. Sci. Lett.* 6 (1997) 769–771.
- [43] Y. Zhao, K. Li, M. Gargani, W. Xiong, A comparative analysis of inconel 718 made by additive manufacturing and suction casting: Microstructure evolution in homogenization, *Addit. Manuf.* 36 (2020) 17–22.
- [44] C.N. Wei, H.Y. Bor, L. Chang, The effects of carbon content on the microstructure and elevated temperature tensile strength of a nickel-base superalloy, *Mater. Sci. Eng. A.* 527 (2010) 3741–3747. <https://doi.org/10.1016/j.msea.2010.03.053>.
- [45] S. Azadian, L.-Y. Wei, R. Warren, Delta phase precipitation in Inconel 718, *Mater. Charact.* 53 (2004) 7–16.
- [46] A. Devaux, L. Naz, R. Molins, A. Pineau, A. Organista, J.F. Uginet, Gamma double prime precipitation kinetic in Alloy 718, *Mater. Sci. Eng. A.* 486 (2008) 117–122. <https://doi.org/10.1016/j.msea.2007.08.046>.
- [47] X. Xie, J. Dong, G. Wang, W. You, THE EFFECT OF Nb, Ti, Al ON PRECIPITATION AND STRENGTHENING BEHAVIOR OF 718 TYPE SUPERALLOYS, *Superalloys 718, 625, 706 Var. Deriv.* 3 (2005) 287–298.
- [48] M.K. Miller, S.S. Babu, M.G. Burke, Comparison of the phase compositions in Alloy 718 measured by atom probe tomography and predicted by thermodynamic calculations, *Mater. Sci. Eng. A.* 327 (2008) 84–88.

- [49] V. Randle, P.R. Rios, Y. Hu, Grain growth and twinning in nickel, *Scr. Mater.* 58 (2008) 130–133. <https://doi.org/10.1016/j.scriptamat.2007.09.016>.